The impact of feedback on the low-redshift intergalactic medium

L. Tornatore,[1,2,3] S. Borgani,[1,2,3] M. Viel[2,3]⋆ and V. Springel[4]

[1]*Dipartimento di Astronomia dell'Università di Trieste, Via G. B. Tiepolo 11, I-34131 Trieste, Italy*
[2]*INAF - Osservatorio Astronomico di Trieste, Via G. B. Tiepolo 11, I-34131 Trieste, Italy*
[3]*INFN/National Institute for Nuclear Physics, Via Valerio 2, I-34127 Trieste, Italy*
[4]*Max-Planck Institut fuer Astrophysik, Karl-Schwarzschild Strasse 1, D-85748 Garching, Germany*

ABSTRACT

We analyse the evolution of the properties of the low-redshift intergalactic medium (IGM) using high-resolution hydrodynamic simulations that include a detailed chemical evolution model. We focus on the effects that two different forms of energy feedback, strong galactic winds driven by supernova explosion and active galactic nuclei powered by gas accretion on to super-massive black holes (BHs), have on the thermo- and chemodynamical properties of the low-redshift IGM. We find that feedback associated with winds (W) and BHs leaves distinct signatures in both the chemical and thermal history of the baryons, especially at redshift $z < 3$. BH feedback produces an amount of gas with temperature in the range of 10^5–10^7 K, the warm-hot intergalactic medium (WHIM), larger than that produced by the wind feedback. At $z = 0$, the fraction of baryons in the WHIM is about 50 per cent in the runs with BH feedback and about 40 per cent in the runs with wind feedback. The number of warm baryons ($10^4 < T < 10^5$ K) is instead at about the same level, $\sim$30 per cent, in the runs with BH and wind feedback. Also, BH feedback provides a stronger and more pristine enrichment of the WHIM. We find that the metal-mass-weighted age of WHIM enrichment at $z = 0$ is on average a factor of $\sim$1.5 smaller in the BH run than for the corresponding runs with galactic winds. We present results for the enrichment in terms of mass and metallicity distributions for the WHIM phase, both as a function of density and as a function of temperature. Finally, we compute the evolution of the relative abundances between different heavy elements, namely oxygen, carbon and iron. While both C/O and O/Fe evolve differently at high redshifts for different feedback models, their values are similar at $z = 0$. We also find that changing the stellar initial mass function has a smaller effect on the evolution of the above relative abundances than changing the feedback model. The sensitivity of WHIM properties on the implemented feedback scheme could be important both for discriminating between different feedback physics and for detecting the WHIM with future far-UV and X-ray telescopes.

Key words: methods: numerical – intergalactic medium – cosmology: theory.

1 INTRODUCTION

Solving the problem of the missing baryons at low redshift is one of the important goals of observational cosmology (e.g. Persic & Salucci 1992; Fukugita, Hogan & Peebles 1998; Fukugita & Peebles 2004). Since the pioneering work by Cen & Ostriker (1999), cosmological hydrodynamic simulations provided a fundamental contribution in this field (see also Davé et al. 2001). Although the baryon budget is closed by observations at high redshift, $z \gtrsim 2$, simulations indicate that about half of the baryons at low-z should lie in a tenuous quite elusive phase, the so-called warm-hot intergalactic medium (WHIM). The WHIM is predicted to be made of low den-

sity ($n_{\rm H} \sim 10^{-6}$–10^{-4} cm^{-3}) and relatively high temperature ($T \sim 10^5$–10^7 K) plasma, whose main constituents are ionized hydrogen and helium, with traces of heavier elements in high ionization states. Simulations have also shown that gas at these densities traces the filamentary structures which define the skeleton of the large-scale cosmic web, and is heated by shocks from supersonic gravitational accretion on to the forming potential wells.

Due to its low density, the collisionally ionized WHIM should be characterized in emission by a very low surface brightness in the UV and soft X-ray bands so that its detection lies beyond the capability of available detectors and should await for instrumentation of the next generation (e.g. Yoshikawa et al. 2004). Claims for the detection of the WHIM through soft X-ray emission have already been presented (e.g. Zappacosta et al. 2005; Werner et al. 2008).

⋆E-mail: viel@oats.inaf.it

However, these detections are limited to special places, such as external regions of massive galaxy clusters or large filaments connecting such clusters, where the gas density reaches values higher than expected for the bulk of the WHIM. A more promising approach to revealing the presence of the WHIM lies in the detection of absorption features in the spectra of background sources, at far-ultraviolet (FUV) and soft X-ray energies, associated with atomic transitions from highly ionized elements, using gamma ray burst (GRB) spectra (Fiore et al. 2000; Branchini et al. 2009), or in the detection of Lyα absorption from the tiny fraction of neutral hydrogen revealed through FUV spectroscopy (see Richter, Paerels & Kaastra 2008, for a review). Although detection of gas with $T < 10^5$ K has been obtained at FUV frequencies along a fairly large number of sightlines (e.g. Tripp et al. 2008, and references therein), the situation is less clear in the soft X-ray band. At these energies, claims of WHIM detection in absorption have been presented by different authors (e.g. Nicastro et al. 2005; Buote et al. 2009), although they are either controversial (e.g. Kaastra et al. 2006; Rasmussen et al. 2007) or have moderate statistical significance.

Owing to the above observational difficulties in detecting and characterizing the physical properties of the WHIM, numerical simulations have played over the last few years a two-fold role to forecast its detectability, both in emission (e.g. Roncarelli et al. 2006; Ursino & Galeazzi 2006) and in absorption (e.g. Cen et al. 2001; Kravtsov, Klypin & Hoffman 2002; Chen et al. 2003; Viel et al. 2003, 2005), and to predict its observational properties, also as a function of the physical processes included (see Bertone, Schaye & Dolag 2008, for a review). For instance, feedback effects from star formation and accretion on to super-massive black holes (SMBHs) are expected to determine at the same time the process of galaxy formation and the physical properties of the diffuse cosmic baryons. However, as of today, the mechanisms powering feedback are still poorly understood and thus very difficult to model in a fully self-consistent way in cosmological hydrodynamical simulations. On the other hand, numerical simulations from different groups (e.g. Cen & Ostriker 2006; Davé & Oppenheimer 2007; Kobayashi, Springel & White 2007; Oppenheimer & Davé 2008; Tescari et al. 2009; Wiersma et al. 2009) confirm that the thermo- and chemodynamical properties of the WHIM and, more generally, of the intergalactic medium (IGM) at different redshifts are sensitive to the nature and timing of the feedback. Indeed, metals are observed in the low-density IGM out to high redshift and it is likely that galactic winds, as observed in galaxies in the low-redshift universe, are responsible for the IGM metal enrichment. Furthermore, SMBHs are also expected to have an impact on the gas distribution in galaxies and to blow ejecta out to large distances, especially during galaxy mergers.

In this paper, we will present an analysis of an extended set of cosmological hydrodynamical simulations with the purpose of investigating the effect that both galactic winds powered by supernova (SN) explosions and energy feedback from accretion on to SMBHs have in determining the thermal and chemical properties of the IGM. Although the main focus of the analysis is on the low-redshift IGM, we will also discuss how different feedback mechanisms leave their imprint on the evolutionary properties of diffuse baryons since $z \sim 4$. Our simulations are based on the chemodynamical version of the GADGET-2 code (Springel 2005) presented by Tornatore et al. (2007), which follows the production of different chemical species by accounting for detailed yields from Type Ia SN and Type II SN (SN-Ia and SN-II hereafter) as well as from intermediate and low mass stars in the thermally pulsating asymptotic giant branch (TP-AGB) phase, while also accounting for the mass-dependent lifetimes with which

different stellar populations release their nucleosynthetic products. The model of galactic winds is that introduced by Springel & Hernquist (2003), which we consider both in its original version and in a version based on assuming that winds are never hydrodynamically decoupled from the surrounding medium (see also Dalla Vecchia & Schaye 2008). As for the BH feedback, we adopt the models originally introduced by Di Matteo, Springel & Hernquist (2005) and Springel, Di Matteo & Hernquist (2005). Besides investigating the effect of different feedback mechanisms, we will also consider the impact of changing the stellar initial mass function (IMF) on the resulting enrichment pattern of the IGM. Although the results of this paper have important implications for the detectability of the WHIM in view of next-generation X-ray missions, we defer an observationally oriented analysis of our simulations to a future work, aimed at investigating in detail how different instrumental capabilities will be able to characterize the WHIM properties at the level required to discriminate between different feedback models.

The plan of the paper is as follows. In Section 2, we describe the hydrodynamical simulations used and the feedback mechanisms adopted. Section 3 describes the main results of our analysis in terms of global gas properties (evolution of different phases over redshift), epoch of enrichment of gas particles, metallicity distributions at $z = 0$ as a function of overdensity and temperatures, and evolution of different chemical elements. We provide a final discussion of our results and draw our main conclusions in Section 4. In the following, we will assume the values of the solar metallicity as reported by Asplund, Grevesse & Sauval (2005), with $Z/X = 0.0165$ (X: hydrogen mass; Z: mass contributed by all elements heavier than helium).

2 HYDRODYNAMICAL SIMULATIONS

Our simulations were carried out using a version of the parallel hydrodynamical TreePM-smoothed particle hydrodynamics (SPH) code GADGET-2 (Springel 2005), which includes a detailed implementation of the chemical enrichment as described in Tornatore et al. (2007). The initial conditions are generated at redshift $z = 99$ in a cosmological volume with periodic boundary conditions filled with an initially equal number of dark matter (DM) and gas particles. The matter power spectrum is generated using CMBFAST (Seljak & Zaldarriaga 1996) for a flat Λ cold dark matter (ΛCDM) model, with cosmological parameters consistent with the recent findings of *Wilkinson Microwave Anisotropy Probe* (*WMAP*) year-5 (Komatsu et al. 2009): $\Omega_{0m} = 0.24$, $\Omega_{0\Lambda} = 0.76$, $\Omega_{0b} = 0.0413$, for the density parameters contributed by total matter, cosmological constant and baryons, respectively, $n_s = 0.95$ for the primordial spectral index, $H_0 = 73 \, \mathrm{km \, s^{-1} \, Mpc^{-1}}$ and $\sigma_8 = 0.8$ for the normalization of the power spectrum. Besides performing simulations within boxes of $37.5 \, h^{-1}$ comoving Mpc using 2×256^3 gas and DM particles, we also run a few simulations within a twice as large box of $75 \, h^{-1}$ Mpc on a side, with 2×512^3 particles so as to keep resolution constant. Such larger boxes will allow us to keep under control any effect related to box size. The resulting mass of the gas particles is thus $m_{gas} \simeq 3.6 \times 10^7 \, h^{-1} \, \mathrm{M_\odot}$. In these runs, the gravitational softening is set to $\epsilon = 7.5 \, h^{-1}$ comoving kpc above $z = 2$, while at $z < 2$ it is set to $\epsilon = 2.5 \, h^{-1}$ physical kpc. As for the B-spline softening length used for the computation of the SPH forces, the lowest value allowed was set to half of the gravitational softening. In order to address resolution effects, we also carried out one simulation in the smaller box using 2×400^3 particles. In this case the mass of the gas particles is $m_{gas} \simeq 9.4 \times 10^6 \, h^{-1} \, \mathrm{M_\odot}$, with all the softening

Table 1. Summary of the different runs.

Run	Box size	$N_{\mathrm{DM}}^{1/3}$	IMF	Feedback
$W_{37,256}$	37.5	256	Kroupa	Winds; $v_{\mathrm{w}} = 500\,\mathrm{km\,s^{-1}}$
$W_{75,512}$	75.0	512	Kroupa	Winds; $v_{\mathrm{w}} = 500\,\mathrm{km\,s^{-1}}$
$W_{37,400}$	37.5	400	Kroupa	Winds; $v_{\mathrm{w}} = 500\,\mathrm{km\,s^{-1}}$
$Way_{37,256}$	37.5	256	Arimoto-Yoshii	Winds; $v_{\mathrm{w}} = 500\,\mathrm{km\,s^{-1}}$
$Ws_{37,256}$	37.5	256	Salpeter	Winds; $v_{\mathrm{w}} = 500\,\mathrm{km\,s^{-1}}$
$NW_{37,256}$	37.5	256	Kroupa	No feedback
$CW_{37,256}$	37.5	256	Kroupa	Coupled winds; $v_{\mathrm{w}} = 500\,\mathrm{km\,s^{-1}}$
$BH_{37,256}$	37.5	256	Kroupa	BH feedback, no winds

Note. Column 1: run name, column 2: comoving box size (units of h^{-1} Mpc), column 3: number of DM particles, column 4: stellar IMF (see text) and column 5: feedback included (see text).

lengths rescaled according to $m_{\mathrm{gas}}^{-1/3}$: $\epsilon = 4.8\,h^{-1}$ comoving kpc at $z > 2$ and $\epsilon = 1.6\,h^{-1}$ physical kpc at lower redshift. All these simulations are evolved to $z = 0$.

We point out that both a large volume and high resolution are necessary in order to correctly describe the physical properties of the WHIM. Indeed, shocks driven by the collapse of large-scale structures are important, while dense environments able to trigger and power the feedback processes need to be resolved. Our simulations of different resolutions and/or box sizes will be denoted by the tuple (linear size of the box in comoving h^{-1} Mpc, number of DM particles$^{1/3}$). For instance, we will indicate with (75 512) a simulation within a box of $75\,h^{-1}$ Mpc and containing 512^3 DM particles (see Table 1).

Radiative cooling and heating processes are followed for a primordial mix of hydrogen and helium, and we include the dependence of cooling on metallicity by adopting the cooling rates from the tables by Sutherland & Dopita (1993). We also include the effect of a spatially uniform redshift-dependent ultraviolet background (UVB) produced by quasars, as given by Haardt & Madau (1996), with helium heating rates multiplied by a factor of 3.3 in order to better fit observational constraints on the temperature evolution of the IGM. This background gives naturally a hydrogen ionization rate $\Gamma_{-12} \sim 0.8$ at $z = 2$–4 (Bolton et al. 2005), which is in broad agreement with the observations. We adopt the effective model of star formation from a multiphase interstellar medium (ISM) introduced by Springel & Hernquist (2003). In this model, each gas particle whose density exceeds a limiting threshold value is assumed to contain a hot and a cold phase, the latter providing the reservoir of star formation. The two phases coexist in pressure equilibrium with their relative fractions being computed according to the local conditions of density and temperature. In our simulations we assume that the density threshold for a gas particle to become multiphase and, therefore, star forming, is $n_{\mathrm{H}} = 0.1\,\mathrm{cm}^{-3}$ in terms of the number density of hydrogen atoms. Star-forming gas particles are then assumed to spawn collisionless gas particles according to the stochastic scheme originally introduced by Katz, Weinberg & Hernquist (1996). We allow each gas particle to produce up to three generations of star particles, each having therefore a typical mass of about one-third of the initial mass of the gas particles.

Our simulations have been carried out with the chemodynamical version of the GADGET-2 code described by Tornatore et al. (2007). The model of chemical evolution included allows us to follow the production of six different metal species (C, O, Mg, S, Si and Fe) from SN-II and SN Ia, along with low and intermediate mass stars (LIMS) in the TP-AGB phase. Besides including different contributions from SN-II, SN-Ia and LIMS, we also include the effect of the mass-dependent time delay with which different stellar popu-

lations release metals. Specifically, we adopt the lifetime function given by Padovani & Matteucci (1993). We use the stellar yields by Thielemann et al. (2003) for SN-Ia, by Woosley & Weaver (1995) for SN-II and by van den Hoek & Groenewegen (1997) for LIMS. The mass range for SN-II is $M > 8\,\mathrm{M}_{\odot}$, while for SN-Ia arising from binary systems the mass range is $0.8 < M/\mathrm{M}_{\odot} < 8$, with a binary fraction of 10 per cent. Finally, we use three distinct stellar IMFs: a Salpeter (1955), a Kroupa (2001) and an Arimoto-Yoshii (1987) IMF. Our reference choice is the functional form proposed by Kroupa (2001) which adopts a multislope approximation, $\varphi(m) \propto m^{-y}$ with $y = 0.3$ for stellar mass $m < 0.5\,\mathrm{M}_{\odot}$, $y = 1.2$ for $0.5\,\mathrm{M}_{\odot} \leq m < 1\,\mathrm{M}_{\odot}$ and $y = 1.7$ for $m \geq 1\,\mathrm{M}_{\odot}$. Both the IMF by Salpeter (1955) and that by Arimoto & Yoshii (1987) have instead a single slope, with $y = 1.35$ and $y = 0.95$, respectively. Our model of chemical evolution also includes stellar mass losses, which are self-consistently computed for a given IMF and lifetime function. This means that a fraction of the mass of the star particles is restored as diffuse gas during the evolution and distributed to the surrounding gas particles. We refer to Tornatore et al. (2007) for a detailed description of our implementation of chemodynamics in GADGET-2 to Saro et al. (2006) and Fabjan et al. (2008) for applications to simulations of galaxy clusters and to Tescari et al. (2009) for a description of the global IGM properties around damped Lyman-α systems (DLAs) at $z > 2$.

In the following two subsections, we will summarize the main features of the two different feedback schemes adopted in this paper.

2.1 Galactic outflows

The implementation of galactic outflows is extensively described by Springel & Hernquist (2003). In this model, winds are assumed to blow from star-forming regions with a mass loading rate $\dot{M}_{\mathrm{w}}$ proportional to the star formation rate (SFR) $\dot{M}_{\star}$ according to $\dot{M}_{\mathrm{w}} = \eta \dot{M}_{\star}$. Star-forming gas particles are then stochastically selected to become part of a blowing wind, with a probability which is proportional to their SFR. In its original implementation, whenever a particle is uploaded to the wind, it is decoupled from hydrodynamics until the density of the surrounding gas drops below a given limiting value. This allows the wind particle to travel 'freely' up to few kpc until it has left the dense star-forming phase, without directly affecting it. As a protection against decoupling a wind particle indefinitely in case it gets 'stuck' in the ISM of a very massive galaxy, the maximum allowed time for a wind particle to stay hydrodynamically decoupled is set to $t_{\mathrm{dec}} = l_{\mathrm{w}}/v_{\mathrm{w}}$, where we fix $l_{\mathrm{w}} = 10\,h^{-1}$ kpc in our reference case, while v_{w} is the wind speed. As for the limiting density for hydrodynamic decoupling of gas particles, it is set to 0.5 in units of the threshold for star formation. Unlike in Springel &

Hernquist (2003), we decide here to fix the velocity of the winds to the value $v_w = 500$ km s^{-1}, instead of fixing the fraction of the SN-II energy powering galactic ejecta. For the efficiency of the wind mass loading, we adopt $\eta = 2$. In sum, four parameters fully specify the wind model: the wind efficiency η, the wind speed v_w, the wind free travel length l_w (whose detailed value is unimportant) and the wind free travel density factor.

In order to verify the effect of the hydrodynamic decoupling of wind particles we also perform a simulation without such a decoupling, $t_{dec} = 0$, i.e. keeping the particles always hydrodynamically coupled. We note that Nagamine et al. (2007) showed that global DLA properties are relatively insensitive to the value of l_w. On the other hand, Dalla Vecchia & Schaye (2008) pointed out that keeping winds always hydrodynamically coupled has a significant effect on the evolution and star formation in simulations of isolated disc galaxies.

We stress that our wind model is not the only possible wind implementation and others could be adopted such as those based on momentum-driven winds as suggested by Murray, Quataert & Thompson (2005) and Davé & Oppenheimer (2007).

2.2 BH feedback

We also include in our simulations the effect of feedback energy from gas accretion on to SMBHs, following the scheme originally introduced by Springel et al. (2005) (see also Di Matteo et al. 2005). In this model, BHs are represented by collisionless sink particles initially seeded in just resolved DM haloes, which subsequently grow via gas accretion and through mergers with other BHs during close encounters. Every new DM halo, identified by a run-time friends-of-friends algorithm, above the mass threshold $M_{th} = 10^{10}\, h^{-1}\, M_\odot$, is seeded with a central BH of initial mass $10^5\, h^{-1}\, M_\odot$, provided the halo does not contain any BH yet. Each BH can then grow by local gas accretion, with a rate given by

$$\dot{M}_{BH} = \min(\dot{M}_B, \dot{M}_{Edd}). \qquad (1)$$

Here $\dot{M}_B$ is the accretion rate estimated with the Bondi–Hoyle–Lyttleton formula (e.g. Bondi 1952) and $\dot{M}_{Edd}$ is the Eddington rate. The latter is inversely proportional to the radiative efficiency ϵ_r, which gives the radiated energy in units of the energy associated with the accreted mass: $\epsilon_r = L_r/(\dot{M}_{BH}c^2)$. Following Springel et al. (2005), we use $\epsilon_r = 0.1$ as a reference value, which is typical for a radiatively efficient accretion on to a Schwarzschild BH (Shakura & Sunyaev 1973). The model then assumes that a fraction ϵ_f of the radiated energy is thermally coupled to the surrounding gas, so that $\dot{E}_{feed} = \epsilon_r \epsilon_f \dot{M}_{BH}c^2$ is the rate of the energy released to heat the surrounding gas. Using $\epsilon_f \sim 0.05$, Di Matteo et al. (2005) were able to reproduce the observed M_{BH}–σ relation between bulge velocity dispersion and mass of the hosted BH (see also Di Matteo et al. 2008; Sijacki et al. 2008). Gas particle accretion on to the BH is implemented in a stochastic way, by assigning to each neighbouring gas particle a probability of contributing to the accretion, which is proportional to the SPH kernel weight computed at the particle position. In the scheme described above, this stochastic accretion is used only to increase the dynamic mass of the BHs, while their mass entering in the computation of the accretion rate is followed in a continuous way, by integrating the analytic expression for $\dot{M}_{BH}$. Once the amount of energy to be thermalized is computed for each BH at a given time-step, this energy is then distributed to the surrounding gas particles using the SPH kernel weighting scheme.

To sum up, we run simulations with the Kroupa (2001) IMF by turning off galactic winds (NW), with galactic winds (W), with

galactic winds always hydrodynamically coupled (CW) and with BH feedback. We summarize in Table 1 the simulations analysed in this paper. Overall, our simulation set allows us to address the effect of changing (i) the box size (by comparing W$_{37,256}$ with W$_{75,512}$ and Way$_{37,256}$ with Way$_{75,512}$), (ii) the IMF (by comparing W$_{37,256}$ with Way$_{37,256}$ and with Ws$_{37,256}$), (iii) the resolution (by comparing W$_{37,256}$ with W$_{37,400}$) and (iv) the nature of the energy feedback (by comparing W$_{37,256}$ with NW$_{37,256}$ and with CW$_{37,256}$ and with BH$_{37,256}$).

3 RESULTS

In Fig. 1 we show the SFRs for the W$_{37,256}$, NW$_{37,256}$, CW$_{37,256}$ and BH$_{37,256}$ simulations along with observational results by Hopkins (2004). At $z \gtrsim 3$, the NW and BH runs behave very similarly. This is not surprising since BH feedback is not effective until a sufficiently large number of DM haloes, massive enough to host a seed BH, is numerically resolved. After that, gas accretion takes place in BHs with a subsequent release of thermal energy. Once BH feedback becomes efficient, star formation is suddenly suppressed by the expulsion of hot gas. Kinetic feedback by galactic winds is relatively more efficient at high redshifts in depriving relatively small haloes of the star-forming gas, while it fails in regulating the star formation within massive haloes at later epochs. We note that hydrodynamically coupled winds (CW) tend to produce a slightly higher SFR around the peak of the star formation history. This is due to the fact that coupled winds tend to thermalize their kinetic energy at smaller distances from star-forming and dense regions. The cooling time of this gas is correspondingly shorter, which causes a larger fraction of the thermalized wind energy to be radiated away, thus reducing the feedback efficiency. Both runs including winds reproduce the observed behaviour of the SFR at high redshift, $z \gtrsim 2$, while they tend to produce too high star formation at low redshift. On the contrary, the run with BH feedback has a too high star formation at $z > 3$, while it recovers the observed SF level at $z \lesssim 2$.
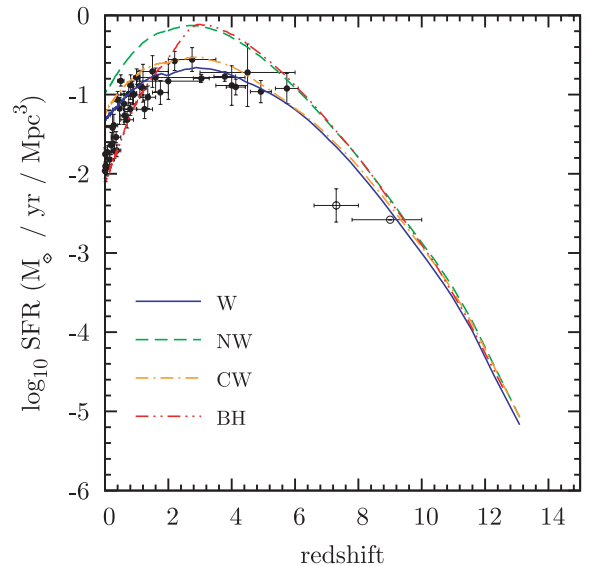

Figure 1. SFR density as a function of redshift in units of M$_\odot$ yr^{-1} Mpc^{-3} for W$_{37,256}$ (winds, continuous blue line), NW$_{37,256}$ (no feedback, dashed green line), CW$_{37,256}$ (coupled winds, dot–dashed orange line) and BH$_{37,256}$ (BH feedback, triple dotted–dashed line) runs. Observational data points represented as full circles are taken from Hopkins (2004), while the empty circles are from Bouwens et al. (2008).
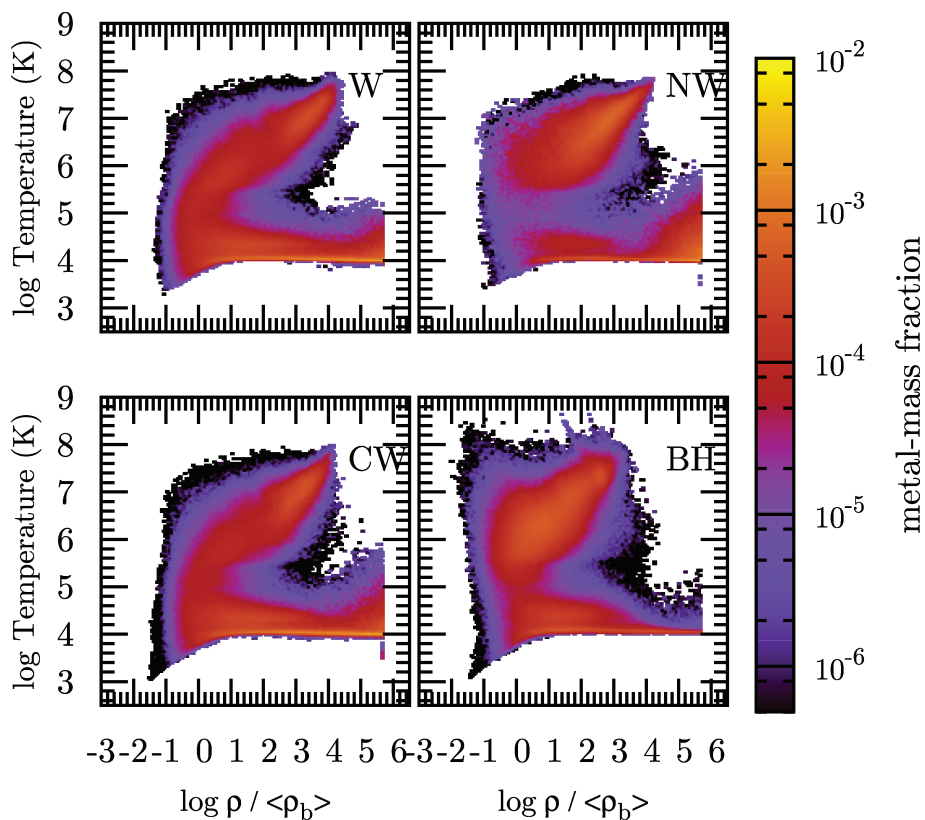
Figure 2. The $\rho_{gas}-T$ phase diagrams at $z = 0$ for simulations based on the Kroupa (2001) IMF, by varying the feedback scheme, colour coded according to the metal mass fraction (see the vertical bar): NW$_{37,256}$ run with no feedback (top left), W$_{37,256}$ run with galactic winds (top right), CW$_{37,256}$ run with galactic winds always hydrodynamically coupled (bottom left) and BH$_{37,256}$ run with BH feedback (bottom right).

This illustrates once again the different roles played by feedback related to star formation and to BH accretion: while the former is efficient since early times in regulating gas cooling within small haloes, the latter sets in at relatively lower redshift to quench star formation within recently formed massive haloes.

3.1 Global gas properties

We show in Fig. 2 the density–temperature phase diagrams for the gas in the four simulations based on the Kroupa (2001) IMF and including different feedback schemes. The four panels are for the simulations without feedback (NW$_{37,256}$, top left), with feedback associated with galactic winds (W$_{37,256}$, top right), with galactic winds always hydrodynamically coupled (CW$_{37,256}$, bottom left) and with BH feedback (BH$_{37,256}$, bottom right). Each phase diagram is colour-coded according to the mass in metals which is associated with the gas particles belonging to each two-dimensional bin in the $\rho_{gas}-T$ plane, with brighter regions corresponding to a larger metal mass. As such, these plots convey information on the effect that different feedback schemes have on the way in which metals are distributed in density and temperature. Here and in the following we do not include in the baryon budget inventory the ISM, i.e. for gas having density larger than the density threshold for the star formation (see Section 2). We note that only a tiny fraction of the gas lies in this phase at all redshifts. Furthermore, while our sub-grid model for star formation should provide an effective description of the ISM, it is not obvious that this description provides a fully realistic description of its temperature. For this reason, our gas mass

and metal budget will not include the contribution from star-forming gas.

The effect of feedback is quite strong for gas in the temperature range of 10^5-10^7 K (corresponding to the WHIM phase that we will define below; e.g. Cen & Ostriker 2006). Strong galactic winds increase the number of metals carried by gas with temperature in the range of 10^5-10^6 K and overdensity[1] $\delta_b \simeq 1-10$, when compared to the no-feedback case. This is a consequence of the fact that winds are loaded with gas particles which were star forming and, as such, have been heavily enriched. The effect is even more dramatic in the presence of BH feedback: even regions below the mean density are enriched with metals up to rather high temperatures ($\sim 10^7$ K) when compared to the corresponding W and CW simulations. This counter-intuitive result follows from the fact that BHs release a large amount of energy in a relatively short time interval, around $z \sim 3$. This sudden energy release turns out to be much more efficient than winds to heat metal-enriched gas to high temperatures, thus displacing it from the haloes of star-forming regions to low-density regions. Once brought to high entropy by BH feedback, this enriched gas is prevented from reaccreting into collapsed haloes at lower redshift. Gas in photoionization equilibrium at $T \sim 10^4$ K contains a comparable number of metals in the three runs which include feedback. In the NW case, the number of metals present in the gas around the mean density is an order of magnitude lower than in the runs including winds. Indeed, in the NW simulation, most of the enriched gas remains at high density, instead of being

---

[1] Here and in the following, we denote with δ_b the overdensity of gas with respect to the mean cosmic baryon density $\bar{\rho}_b$, i.e. $\delta_b = \rho_b/\bar{\rho}_b - 1$.
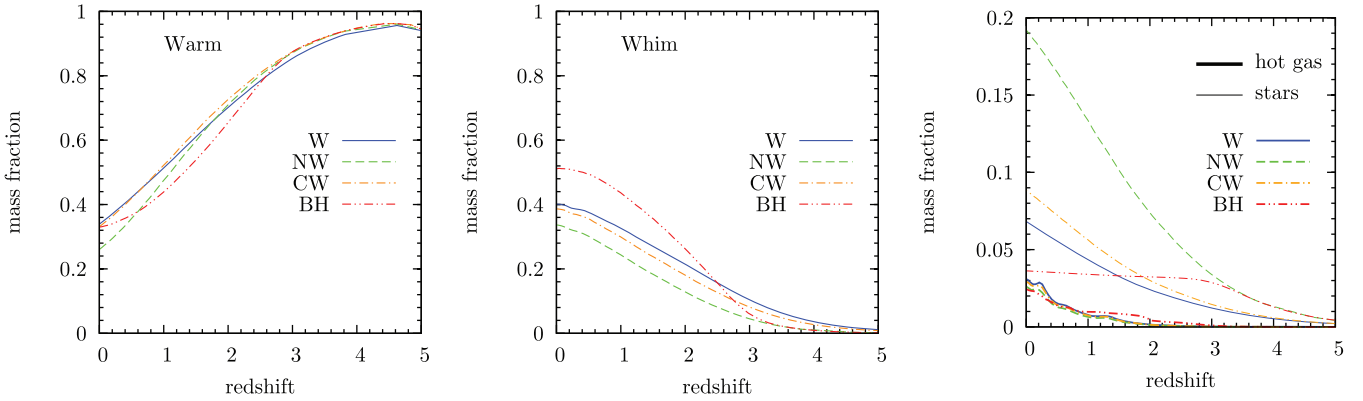
Figure 3. The fraction of mass in the warm (left-hand panel), WHIM (middle panel) and stellar plus hot phases (right-hand panel, thin lines for stars and thick lines for hot gas) as a function of redshift for the $NW_{37,256}$, $W_{37,256}$, $CW_{37,256}$ and $BH_{37,256}$ runs (continuous blue, dashed green, dot–dashed orange and double-dot–dashed red curves, respectively).

transported away from star-forming regions. The short cooling time of this enriched gas causes its selective removal from the diffuse phase into the stellar phase. We also note that relatively cold gas in very dense regions, $\rho_{gas} \simeq (10^3–10^4)\bar\rho_b$, is more enriched with metals in the NW, CW and W simulations than in the BH one. This demonstrates the efficiency of BH feedback in displacing highly enriched gas outside the core regions of virialized haloes, while correspondingly increasing the enrichment level of gas at lower density. As for the comparison between coupled and decoupled winds (W and CW runs, respectively), the latter has more enriched gas at densities approaching the threshold for the onset of star formation. This is the consequence of the hydrodynamic coupling of winds which causes wind particles to remain more confined in the proximity of star-forming regions.

From a qualitative inspection of Fig. 2, we draw the following conclusions: (i) galactic winds have a large impact on the metal enrichment of the IGM at $z = 0$ for both underdense-cold and mean density-hot regions of the $T–\rho_{gas}$ plane; (ii) AGN feedback is more efficient than winds in enriching the warm-hot gas at $T = 10^5–10^7$ K and relatively low overdensity, $\delta_b \lesssim 50$; (iii) correspondingly, very dense regions, with overdensity $\delta_b > 10^4$, are less enriched with metals in the BH simulations than in the other runs.

3.2 Redshift evolution of the different phases

In order to make our results directly comparable with those from previous analyses (e.g. Davé et al. 2001; Cen & Ostriker 2006), we define four different phases for the baryons in our simulations: a WHIM phase, for gas particles with temperature in the range of $10^5–10^7$ K; a warm phase, for gas particles with $T = 10^4–10^5$ K; a hot phase, for gas particles with $T > 10^7$ K; and a condensed phase, which includes all the baryonic mass associated with star particles.

In Fig. 3, we show the redshift evolution of the mass fraction in these four different phases, comparing the effect of changing the feedback scheme. The $W_{37,256}$, $NW_{37,256}$, $CW_{37,256}$ and $BH_{37,256}$ runs are represented by the continuous blue, dashed green, dot–dashed orange and double-dot–dashed red lines, respectively. The warm phase is reported in the left-hand panel. Although showing slightly different evolutions in detail, the amount of warm gas at $z = 0$ is almost the same, $\simeq 35$ per cent, for the runs with galactic winds and with BH feedback. This gas should be partly responsible for local Lyman α forest absorption (e.g. Danforth & Shull 2008), samples the outskirts of galactic haloes and is weakly sensitive to

the energetics and mass-loading parameters of the energy-driven galactic wind feedback (Pierleoni, Branchini & Viel 2008). The case with no feedback (NW) has instead an $\sim$10 per cent lower amount of warm gas at $z = 0$. In the middle panel, we show the evolution of the WHIM phase: with BH feedback the amount of WHIM at $z = 0$ reaches 50 per cent, about 10 per cent more than for the runs with winds and 15 per cent higher than for the NW case. Similar to the results for the warm phase, there are small differences between the W and CW runs, also in the amount of WHIM gas and stars. A more significant difference between W and CW runs is found for the mass fraction in stars. The reason for this difference is in the lower efficiency of the CW feedback model. Indeed, hydrodynamically coupled winds deposit kinetic energy through hydrodynamical processes in relatively higher density environments, which are characterized by shorter cooling times, which causes the thermalized energy to be promptly radiated away.

The evolution of the WHIM mass fraction in the BH run is initially identical to that for the NW run at $z \gtrsim 3.5$. Indeed, at high redshift there is still a limited number of DM haloes whose mass is large enough to host actively accreting BHs. At lower redshift, when accretion on to BHs is more effective, the released feedback energy efficiently heats the gas surrounding galaxy-size haloes, thus moving gas from the warm to the WHIM phase. This explains at the same time the lower amount of warm gas in the BH run at intermediate redshift and the correspondingly larger amount of WHIM. As for the effect of galactic winds, they play a role in heating circumgalactic gas already at high redshift, soon after the onset of star formation. This explains the larger amount of WHIM at $z \gtrsim 2.5$ in the W and CW runs with respect to the BH run. The situation is reversed at lower redshift, when the depths of the forming potential wells become large, making gas heating with winds less effective with respect to BH feedback.

In the right-hand panel we plot the evolution of the mass fractions in stars and hot gas, which are represented by the thin and thick lines, respectively (note the different scale in the y-axis). As expected, the mass in stars in the runs with and without feedback is significantly different, largely reflecting the behaviour of the SFR histories shown in Fig. 1: the BH run has a fraction of stars which is five (two) times less than the NW (CW) run, as a consequence of the quenching of star formation taking place around $z = 3$, while the W run produces a slightly smaller number of stars when compared to the CW one.

Recently, Li & White (2009) used the Sloan Digital Sky Survey (SDSS) data to reconstruct the galaxy stellar mass function in the

local Universe. Assuming an IMF by Chabrier (2003) [very close to the IMF by Kroupa (2001) used in the simulations shown in Fig. 3], they concluded that 3.5 per cent of the baryonic mass are locked into stars. While clearly ruling out a model with no feedback, this observational estimate of the stellar mass fraction is close to the predictions of the BH run, although the SFR in this case is too high at $3 \lesssim z \lesssim 6$ and slightly too low at $z \lesssim 0.5$. As for the W and CW runs, they produce about two times and 2.5 times more stars than the BH run, irrespectively, as a consequence of a star formation excess below $z \sim 1$. These results suggest that both feedback mechanisms should be active: SN-driven galactic ejecta should regulate star formation already at high redshift within relatively small galaxies while BHs should quench cooling in large haloes around the maximum of the star formation, thereby keeping gas pressurized within such haloes down to $z = 0$.

The amount of hot gas at temperatures above 10^7 K is instead very similar for all the simulations and around 3 per cent. This is a consequence of the fact that the bulk of hot gas lies within groups and clusters of galaxies, whose gas content is marginally affected by the details of the feedback. We note, however, that while the amount of hot gas in the BH run is larger than in the other runs at high redshift, it drops below them at $z = 1$, with an overall trend that is opposite to that of the WHIM component. Indeed, at high-redshift BH feedback is quite efficient in heating gas to high temperature, thus providing a sort of diffuse pre-heating. At later time, this pre-heated gas has a harder time to fall into group-size potential wells. To quantify this effect, we note that in the BH run about ~ 10 per cent of the hot gas lie below $\delta_b \sim 1$, while only $\lesssim 0.1$ per cent of hot gas lie at such low densities in the other runs.

It is worth pointing out that although at $z = 0$ the total amount of hot gas is about the same, $\simeq 3$ per cent, for all feedback models, its distribution as a function of density has a distinct pattern in the BH run. In fact, in the runs with no BH feedback gas is heated mostly by the process of gravitational virialization within the potential wells of galaxy groups and clusters. As a consequence, in those runs only about 5 per cent of hot gas lie below virial overdensities, $\delta_b \sim 50$. On the other hand, a sizeable amount of gas displaced by BH feedback lies outside virialized haloes, with ~ 37 per cent of it found at $\delta_b \lesssim 50$. Furthermore, the heating efficiency of BH feedback prevents hot gas from reaching densities as high as in the other runs in the central regions of galaxy groups and clusters (see also Sijacki et al. 2007; Bhattacharya, di Matteo & Kosowsky 2008; Fabjan et al. 2009). As a result, the highest density reached by hot gas in the BH

runs is lower by about a factor of 3 than in the NW, W and CW runs.

Interestingly, hot metals follow the fate of the gas they are associated with. Indeed, the fractions of hot metal mass lying at different densities are quite similar to the corresponding fractions of hot gas mass.

In order to verify the robustness of our results against box size and numerical resolution, we compare in Fig. 4 the results of the $W_{37,256}$ run with those of the $W_{75,512}$ and $W_{37,400}$ runs. In general, we find that there is a very good convergence in the values of the mass fractions associated with the WHIM, warm and star phases, at all considered redshifts. We only note that the amount of gas in the hot phase significantly increases in the $W_{75,512}$ run at $z \lesssim 1.5$. This is due to the fact that a larger box can accommodate a larger number of relatively more massive galaxy groups and clusters where a larger amount of gas is shock-heated to a temperature above 10^7 K. A larger box, with a size of $\sim 200 \, h^{-1}$ Mpc, would certainly allow us to better sample the high end of the halo mass function and, therefore, to provide a fully converged estimate of the mass fraction in hot gas. We note, however, that our larger simulation box already allows us to sample the scale of galaxy groups, which contain gas at a temperature of $\gtrsim 10^7$ K. Indeed, the largest halo found within the $75 \, h^{-1}$ Mpc box has a mass of about $3 \times 10^{14} \, h^{-1} \, M_\odot$ and a X-ray emission-weighted temperature of about 4×10^7 K. Therefore, we do not expect our baryon inventory in simulations to be significantly affected by effects of the finite box size. In the following, we will restrict our analysis to the four (37, 256) runs, based on the four feedback schemes (NW, W, CW and BH). For this reason, and unless otherwise specified, we omit from now on the box size and number of the particles when referring to the analysed simulations.

In summary, we conclude that at $z = 0$ the amount of mass in the WHIM in the simulation including BH feedback is about 10 per cent larger than in the simulations including galactic winds, and also displays a different redshift evolution. Quite remarkably, this result is in quantitative agreement with that reported by Cen & Ostriker (2006). The fact that comparable values for the WHIM mass fraction are found with different simulation codes, based on different hydrodynamic schemes, and using different implementations of feedback processes highlights that this should be considered as a robust prediction of models of cosmic structure formation. Therefore, if future observations will falsify these predictions, this will have direct implications on the need to include new physical processes in simulations.
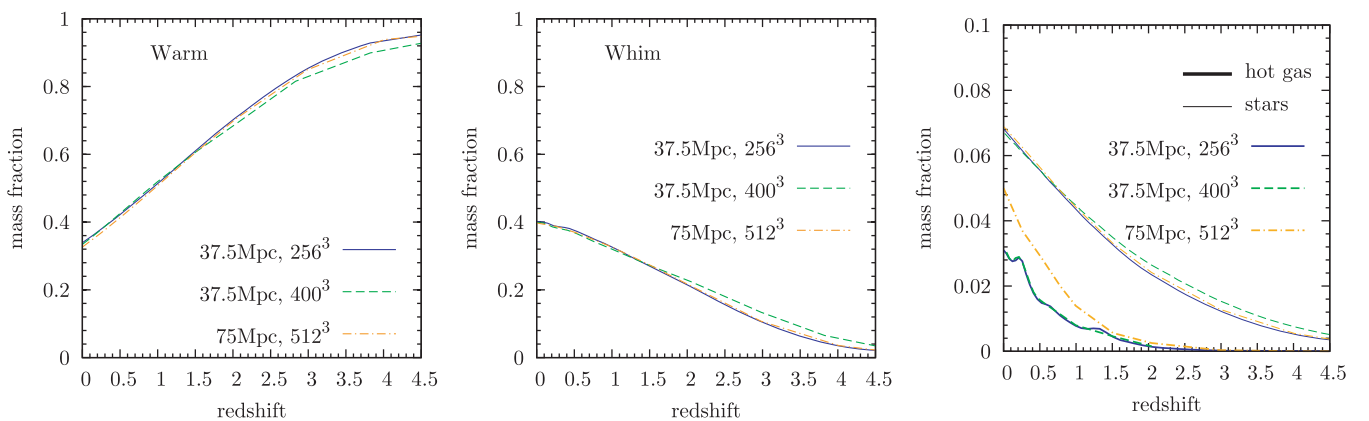
Figure 4. Effects of resolution and box size on the amount of gas in different phases. The fraction of mass in the warm (left-hand panel), WHIM (middle panel) and stars plus hot components (right-hand panel, thin lines for stars and thick lines for hot gas) as a function of redshift for the $W_{37,256}$, $W_{37,400}$ and $W_{75,512}$ runs (continuous blue, dashed green, dot–dashed orange curves, respectively).

3.3 The history of enrichment

In Fig. 5, we show the redshift dependence of the average age of enrichment of the gas particles in units of the age of the universe at the same redshift. Results are shown for warm and WHIM phases. Besides showing results for all gas particles belonging to each of these two phases, in the following we will also classify gas within each phase according to its overdensity. Specifically, we will define a *collapsed* phase, which is made up by all gas particles having overdensity $\delta_b > 50$ (we note that this is the typical overdensity reached within virialized haloes), and a *diffuse* phase, which contains gas at $\delta_b < 50$.

Furthermore, we define the average age of enrichment of a gas particle at redshift z as

$$\bar{t}(z) = \frac{\sum_i \Delta m_{Z,i}(z) t_i}{m_{Z,i}(z)}, \qquad (2)$$

where the sum is over all the time-steps performed until redshift z, $\Delta m_{Z,i}$ is the mass in metals received by the particle at the ith simulation time-step, t_i is the cosmic time at that time-step and $m_Z(z)$ is the total metal mass received by a particle before z. According to this definition, large values of enrichment age, at a given redshift, correspond to a smaller look-back time for the epoch of enrichment, while smaller values of $\bar{t}(z)$ indicate a more pristine metal enrichment. In the limit in which all the metals were received by the particles at the considered redshift z, then the enrichment age coincides with the cosmic age at that redshift. The mean of the ages of enrichment of a given phase is then computed by averaging equation (2) over all particles belonging to that phase, each particle being weighted according to its mass in metals:

$$\bar{t}_{\text{phase}}(z) = \frac{\sum_j \bar{t}_j(z) m_{Z,j}(z)}{\sum_j m_{Z,j}(z)}. \qquad (3)$$

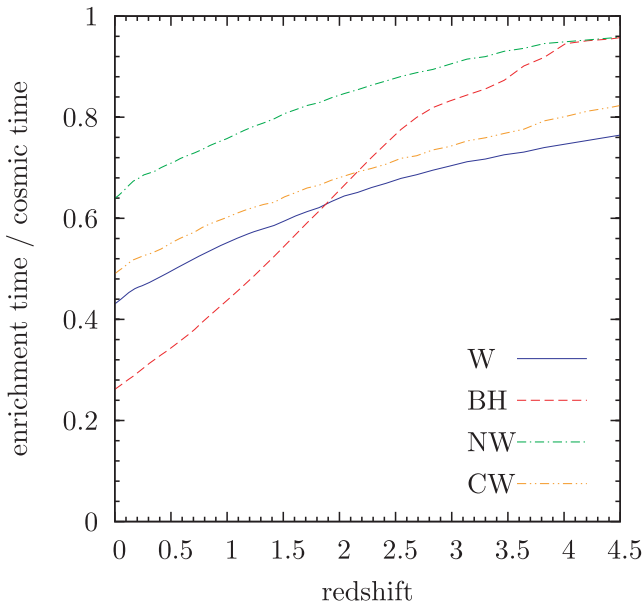It is worth pointing out that this way of computing the enrichment age of a gas phase does not provide a measurement of the average time of enrichment of the phase to which the particles belong; instead, it is an estimate of the average time at which the metals that belong to that phase were deposited in the gas particles currently making up that phase. Fig. 5 shows the redshift dependence of the age of enrichment: the left-hand panel shows the enrichment epoch of the WHIM phase in units of cosmic time at the same redshift, $\bar{t}_{\text{phase}}(z)/t_{\text{cosmic}}(z)$, for the same simulations of Fig. 2.

Fig. 5 shows the enrichment epoch of the WHIM phase. We note that it decreases with time in all runs, thus implying that at high redshifts the metal mass deposition takes place at a larger fraction of the cosmic time. Thus, the lower the value of $\bar{t}_{\text{phase}}(z)/t_{\text{cosmic}}(z)$, the earlier the enrichment of the particles belonging to that phase happened. We also point out that the rate at which the ratio $\bar{t}_{\text{WHIM}}(z)/t_{\text{cosmic}}(z)$ decreases with redshift provides a measure of when the bulk of metals is received by the particles belonging to each phase. For the NW simulation, the WHIM enrichment is always quite recent and is due to the combined action of star formation and structure formation: while the former sets the time-scale at which metals are produced and assigned to the gas surrounding star-forming regions, the latter determines the epoch at which potential wells are sufficiently developed for gas-dynamical processes to become effective in removing gas from such regions during the hierarchical assembly of structures. The W and CW runs exhibit a redshift dependence that is quite similar to that of the NW run. This is not surprising since the wind mass load that carries the metals to the WHIM phase is also proportional to the SFR, while gas-dynamical processes dominate at low redshifts, when the SFR drops at a similar rate in all these runs. A significantly different history of enrichment is instead found in the BH run. In this case, the sudden episodes of energy release, occurring around $2 \lesssim z \lesssim 4$ when the mass accretion rate on to BHs peaks, are very effective in heating and expelling a large amount of enriched gas from the galaxies. Indeed, the faster decrease of the $\bar{t}_{\text{WHIM}}(z)/t_{\text{cosmic}}(z)$ ratio for the simulation with BH feedback is a consequence of the different timing of the enrichment episodes of the particles that then ended in the WHIM. Therefore, while winds produce an enrichment which starts earlier and proceeds more gradually, AGN-BH feedback heats and enriches the particles at later epochs and over a shorter time interval. On the other hand, the lack of feedback capable to displace enriched gas in the NW run delays the release of metals from star-forming regions and closely links the timing of enrichment for WHIM and warm phases to the timing of growth of large potential wells, where stripping of enriched gas from merging haloes takes place.

Another useful diagnostic to study the enrichment timing of the IGM is represented by the relative delays of enrichment between the WHIM and warm phases and between the *diffuse* and *collapsed* environments. We recall that we defined a gas particle to belong to the diffuse phase whenever it has density contrast $\delta_b < 50$, while it belongs to the collapsed phase for $\delta_b > 50$.

In the left-hand panel of Fig. 6 we plot $\bar{t}_{\text{WHIM}, \delta_b < 50} - \bar{t}_{\text{warm}, \delta_b < 50}$, while the right-hand panel shows $\bar{t}_{\text{WHIM}, \delta_b > 50} - \bar{t}_{\text{warm}, \delta_b > 50}$. As shown in this panel, at high redshifts the enrichment of the diffuse WHIM phase in the NW run is on average roughly coeval to that of the diffuse warm phase, while it becomes progressively more recent at lower redshifts (by ~ 0.2 Gyr at $z \sim 2$ and by ~ 1 Gyr at $z = 0$). As already mentioned, this evolution is purely driven by gas-dynamical processes which bring metals from merging haloes to the diffuse medium, whenever these haloes enter the pressurized medium permeating large potential wells. Since enriched gas is extracted from galaxies and groups of galaxies at temperatures typically hotter than that of the IGM, cooler diffuse enriched particles need more time to
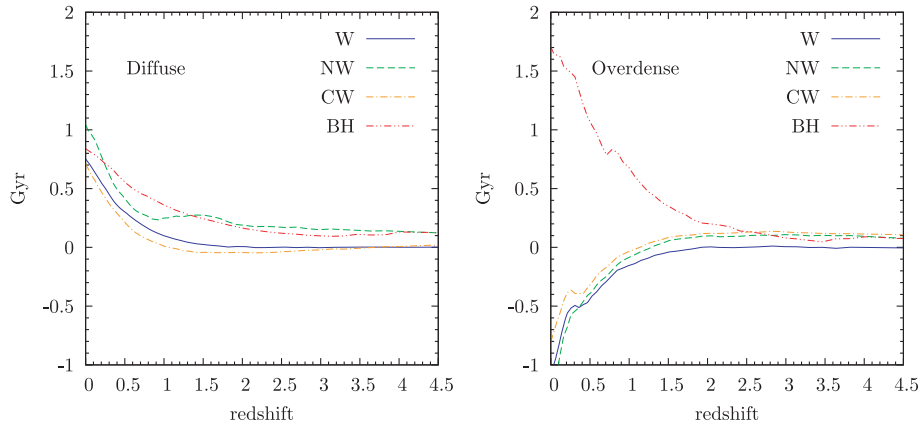

Figure 5. Ratio of the average age of WHIM enrichment to the age of the universe as a function of redshift ($\bar{t}_{\text{WHIM}}/t_{\text{cosmic}}$). Results are shown for the W$_{37,256}$, NW$_{37,256}$, CW$_{37,256}$ and BH$_{37,256}$ simulations, represented by the continuous blue, dot–dashed green, double-dot–dashed orange and dashed red lines, respectively.

Figure 6. Left-hand panel: difference, in Gyr, between the average ages of enrichment for WHIM and warm particles in the diffuse phase ($\bar{t}_{\mathrm{WHIM}, \delta_{\mathrm{b}} < 50} - \bar{t}_{\mathrm{warm}, \delta_{\mathrm{b}} < 50}$). Right-hand panel: the same as in the left-hand panel but for gas in the collapsed phase ($\bar{t}_{\mathrm{WHIM}, \delta_{\mathrm{b}} > 50} - \bar{t}_{\mathrm{warm}, \delta_{\mathrm{b}} > 50}$). Results are shown for the W$_{37,256}$, NW$_{37,256}$, CW$_{37,256}$ and BH$_{37,256}$ simulations, represented by the continuous blue, dot-dashed green, double-dot–dashed orange and dashed red lines, respectively.

reach lower temperatures. This implies that they have been stripped earlier than hotter gas, thus explaining why warm diffuse gas has been enriched before WHIM diffuse gas.

Quite interestingly, the presence of galactic winds (W and CW runs) is effective in improving the mixing between the warm and WHIM diffuse phases, thus making their enrichment coeval down to lower redshifts, $z \simeq 1$. At lower redshifts, gas stripping within large structures again becomes the dominant process, thus recovering the same qualitative behaviour as in the NW run. As for the run with BH feedback, its behaviour is quite close to that of the NW run at high redshifts. At $z \lesssim 3$ gas, displacement from already enriched haloes to the WHIM phase becomes gradually more efficient, thus making the enrichment of the diffuse WHIM more recent than for the diffuse warm gas.

As for the gas in the collapsed phase ($\delta_{\mathrm{b}} > 50$, right-hand panel), the enrichment of the warm and of the WHIM phases is almost coeval down to $z \simeq 2$ in the NW run. The reason for this lies in the relatively short time-scale over which warm particles within haloes are heated to $T > 10^5$ K and enriched when they approach star-forming regions. At lower redshift, the growth of progressively larger structures makes gas in a shock-heated phase to have a progressively higher temperature, until it eventually reaches the WHIM temperature range. At $z = 0$ this gas makes up a phase with $T > 10^5$ K, reaching an overdensity of up to $\delta_{\mathrm{b}} \sim 10^4$, as shown in the upper left-hand panel of Fig. 2. Differently from the warm dense gas, the shock-heated WHIM does not lie close to star-forming regions and, as such, it did not experience recent enrichment episodes. By $z = 0$, the enrichment age of the WHIM takes place on average $\gtrsim 1$ Gyr earlier than that of warm gas. As for the W run, we note that the effect of winds is that of shortening the time-scale that warm gas takes to reach WHIM temperatures, thereby making even more coeval the enrichment age of the diffuse and collapsed phases. The run with BH feedback is again very close the NW run at $z \gtrsim 3$. At lower redshift, BH accretion becomes efficient. The subsequent energy feedback causes a fast removal of recently enriched gas from the very dense warm phase, with $\delta_{\mathrm{b}} > 10^4$, surrounding star-forming regions. This effect is visible in Fig. 2: comparing upper left-hand and lower right-hand panels, one clearly notes the depletion of dense and warm gas in the BH run. This gas is shock heated to larger temperatures, thus providing a supply of recently enriched medium to the WHIM phase.

In general, these results show that the timing of enrichment of the WHIM does depend on the nature of the feedback included in the simulations. The presence of winds leaves its fingerprint in the timing of enrichment of the diffuse component, with $\delta_{\mathrm{b}} < 50$, at relatively high redshift, $z \gtrsim 1$. On the other hand, BH feedback has a much more evident effect at relatively low redshift, $z \lesssim 2$, i.e. in the regime where it reaches the peak of efficiency in quenching star formation and in displacing gas from star-forming regions. Quite interestingly, the effect is more pronounced for the collapsed gas phase, $\delta_{\mathrm{b}} > 50$. This suggests that studying the enrichment pattern of galaxy clusters and groups, out to their outskirts, should represent the best diagnostic for the role played by AGN feedback in determining the cosmic cycle of metals (e.g. Fabjan et al. 2009).

3.4 Properties of the WHIM in the local Universe

3.4.1 Total and metal mass distribution as a function of density and temperature

While in the previous sections we analysed the evolution of different phases, defined according to temperature criteria, we now present an analysis of the metal and gas content of the WHIM at $z = 0$ as a function of gas density and temperature. As such, this analysis has implications for the detectability of the WHIM in the local Universe and for connecting its properties to the feedback mechanisms which determine its density and metallicity structure. The results are presented in Figs 7 and 8 for the density and temperature distributions, respectively. In the left-hand panels of these figures we show the probability distribution function (PDF) for the total WHIM mass, while in the right-hand panels we show the corresponding PDF for the metal mass in the WHIM. These PDFs are defined so that they provide the fraction of WHIM gas mass (metal mass) contributed by unit logarithmic intervals in gas density (Fig. 7) and temperature (Fig. 8).

Consistently with the phase diagrams shown in Fig. 2, the left-hand panel of Fig. 7 shows that the BH feedback predicts a mass distribution for the WHIM component which is quite different from the other simulations: it reaches smaller underdensities, while the high-density tail is suppressed. The reason for this is that this feedback model provides episodes of strong heating of the gas around BHs, allowing it to reach low-density regions, thus reducing the
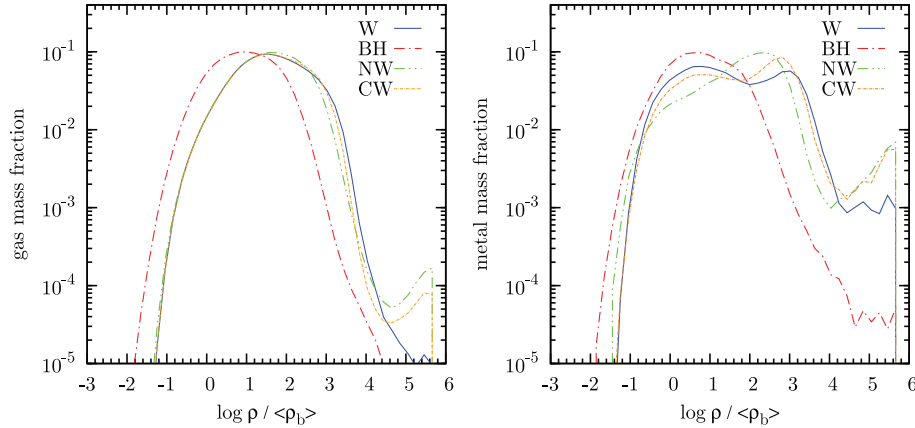
Figure 7. PDF of the total WHIM mass (left-hand panel) and WHIM mass in metals (right-hand panel) at $z = 0$ as a function of gas density (in units of the mean cosmic baryon density) for the W, NW, CW and BH simulations, represented by the continuous blue, dot–dashed green, double-dot–dashed orange and dashed red lines, respectively.
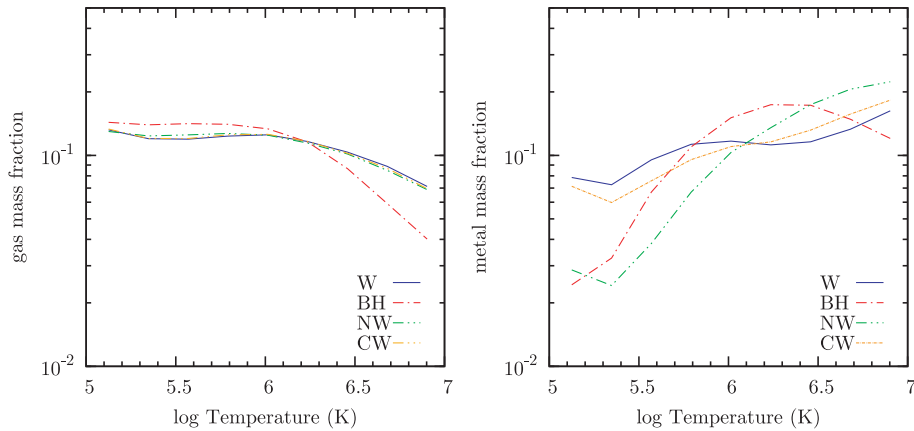

Figure 8. PDFs of the total WHIM mass (left-hand panel) and WHIM mass in metals (right-hand panel) at $z = 0$ as a function of gas temperature for the W, NW, CW and BH simulations, represented by the continuous blue, dot–dashed green, double-dot–dashed orange and dashed red lines, respectively.

gas content of virialized haloes. At $z = 0$, we find that $\sim$50 per cent of the WHIM in the NW, W and CW runs has $\delta_b < 50$, thus lying outside collapsed structures. This fraction increases to $\gtrsim$80 per cent in the run with BH feedback. Correspondingly, the peak of the WHIM density distribution in the BH case lies at $\delta_b \simeq 10$, a value that increases to $\delta_b \simeq 80$ in the other simulations. This result is in line with that found by Bhattacharya et al. (2008) and Puchwein, Sijacki & Springel (2008), who showed that BH feedback is effective in removing gas from virialized haloes having masses typical of galaxy groups. Differences between the W, CW and NW runs are instead more prominent in the high-density tail of the distribution, $\delta_b > 10^4$, where they involve in any case only a tiny fraction of the total WHIM mass. In the NW and CW runs, gas accumulates around star-forming regions, reaching densities close to the threshold density for the onset of star formation. The effect of the decoupled winds in the W run is that of efficiently removing this gas and bringing it to lower density regions, with $\delta_b \simeq 10^3$–10^4.

Similar features that describe the WHIM mass distribution are also visible in the distribution of the mass in metals (right-hand panel of Fig. 7). Metals are more likely found at overdensity $\delta_b \sim 10$ in the BH simulation, while for the NW case this overdensity is usually between 10^2 and 10^3. Again, this comparison clearly shows

that BH feedback is highly efficient in displacing metal-enriched gas from high-density regions, thereby providing a more uniform enrichment of the WHIM at $z = 0$. The PDFs for the CW and W runs have a sort of double-peaked shape: one peak is at moderate overdensity, $\delta_b \sim 10$, that corresponds to the WHIM lying outside virialized haloes, where winds typically deposit metal-enriched gas, and the second peak is at $\delta_b \sim 10^3$, well inside virialized haloes and close to star-forming regions. Such a double-peak structure is more evident for the W run, where winds are more efficient in escaping high-density regions. Finally, we note that in the BH case the metal mass fraction at $\delta_b > 10^2$ is dramatically smaller (by up to two orders of magnitude) than in all the other cases.

As for the temperature distribution of the WHIM, shown in the left-hand panel of Fig. 8, we find that winds have a negligible effect. For BH feedback, it has the effect of reducing the mass fraction of gas above 10^6 K, while correspondingly increasing the fraction of gas at lower temperature. Indeed, BH feedback is efficient in removing gas from haloes having virial temperature within the WHIM range. After being heated by BH feedback, this gas leaves the halo potential wells and cools to lower temperature, $T < 10^5$ K, by adiabatic expansion.

In general, the left-hand panels of Figs 7 and 8 highlight the fact that the presence of galactic winds has a negligible impact
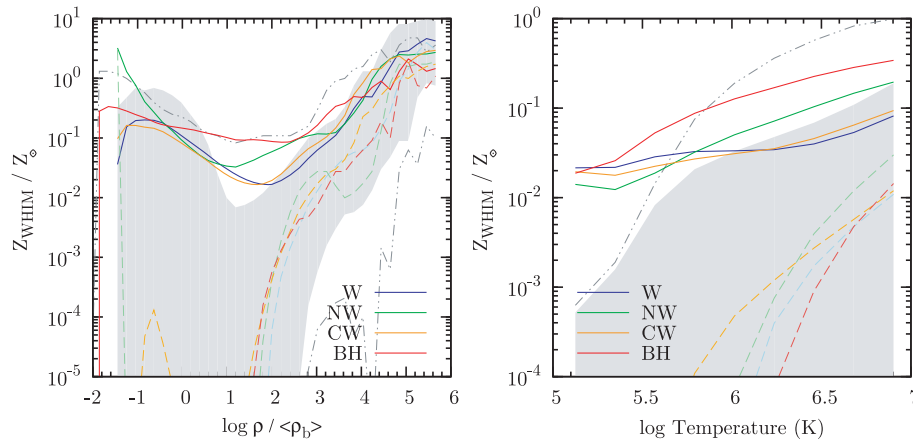
Figure 9. Total metallicity of the WHIM (gas particles at temperatures of 10^5–10^7 K) in solar units at $z = 0$, as a function of gas density (in units of the cosmic mean baryon density $\langle \rho_b \rangle$, left-hand panel) and temperature (right-hand panel). In each panel, the grey shaded area encompasses the 10 and 90 percentiles of the W run, while the dot–dot–dashed lines show the same percentiles for the BH run. Thick coloured lines show the average metallicities while thin dashed lines show the median metallicities.

on the distribution of gas mass in both density and temperature. Although the presence of BHs has a more apparent effect on the distributions of gas mass, it is clear that the distributions of metal mass fractions are much more sensitive to the adopted feedback model (see the right-hand panels of Figs 7 and 8). This is not surprising, since feedback mostly impacts the gas surrounding star-forming regions, which has a higher enrichment level. In the NW run, the metal mass fraction in gas at the low-temperature boundary of the WHIM phase, $T \gtrsim 10^5$ K, is about one order of magnitude lower than for the hot WHIM at $T \lesssim 10^7$ K. The effect of winds is that of transporting metal-rich gas from high-density regions, where it reaches high temperature, to lower density regions, where it cools down by adiabatic expansion. As expected, hydrodynamically coupled winds (CW) make it harder for the gas to leave the densest regions, thus producing a distribution which is intermediate between those of the NW and W runs.

3.4.2 The distribution of the WHIM metallicity

Having characterized how the mass in gas and in metals is distributed as a function of the WHIM density and temperature, we now describe how the WHIM metallicity depends on density and temperature. This characterization of the WHIM is more observationally oriented. Indeed, different distributions of metallicity determine what are the best tracers (chemical elements and their ionization states) to reveal the presence of the WHIM and characterize its physical properties: the presence of different ionization species, that are thought to be the best WHIM tracers, depends in fact upon local conditions of density, temperature and ionization field (see Richter et al. 2008, for a review).

We show in Fig. 9 the distribution of the total metallicity as a function of density within the WHIM temperature range (left-hand panel) and as a function of temperature (right-hand panel). Since the metallicity distributions have always a quite large scatter, a meaningful way of presenting the results is in terms of the mean (continuous lines), median (dashed lines) and of the 10 and 90 percentiles (shaded area for the W run, dot–dot–dashed lines for the BH run) of these distributions. For reasons of clarity, we do not report in these figures the scatter for the NW and CW runs.

As for the density dependence of metallicity in the W, CW and NW simulations (upper left-hand panel), we note that at overdensi-

ties between 10 and 100, which is the range where the PDF of the WHIM mass distribution reaches its maximum value (see Fig. 7), the median metallicity has a strong positive correlation with gas density and increases from $\log (Z/Z_\odot) \simeq -6$ to $\log (Z/Z_\odot) \simeq -2$. Furthermore, the overall scatter around these median values is about two orders of magnitude so that metallicity values as large as $0.1\,Z_\odot$ are not unlikely. An obvious observational implication of this large scatter in the metallicity distributions is that a fairly large number of lines of sight are required in order to better measure the WHIM metallicity and to properly populate such a scatter. It is worth mentioning that the large difference between the average and median metallicities in regions with $\delta_b \lesssim 1$ arises from the highly skewed distribution of metallicity in this regime: most of the underdense gas is not enriched at all, while metals mainly lie in a small number of highly enriched particles with $Z \gtrsim 0.01$. This is mostly true for BH and NW runs, while in W and CW runs the distribution of metals with particle metallicity is significantly shallower. We point out that highly enriched particles preserve their metal content due to the intrinsic lack of diffusivity of the SPH. Including an explicit description of metal diffusion (e.g. Greif et al. 2009) would make such particles sharing their metal content with the surrounding metal-poor particles.

As for the metallicity distribution as a function of temperature (bottom panels), we note a clear trend for metallicity to increase with temperature in all cases, although the details of this trend have a dependence on the feedback model. The median metallicities in the W, CW and NW runs (bottom left-hand panel) increase from 10^{-4}–10^{-3} to $\gtrsim 10^{-2}\,Z_\odot$ as the temperature increases from 10^6 to 10^7 K. The NW simulation predicts a metallicity of the hottest WHIM, with $T \simeq 10^7$ K, which is higher by about a factor of 3 than for the W and CW runs. This gas is located within the virialized regions of galaxy group haloes, which have typical overdensities of about 10^2–10^3 (see the upper left-hand panel). In the NW run, this gas, which remains at these overdensities for a relatively long time before being stripped, has been more heavily enriched by the more (in fact, exceedingly) intense star formation. Quite interestingly, the CW simulation instead shows larger median metallicity at temperatures of $10^{5.5}$–10^6 K, with a shallower decline towards lower temperatures. Gas at this temperature is a mixture of highly enriched gas in virialized haloes and of poorly enriched gas at low density. As can be inferred from the phase diagrams shown in Fig. 2,

gas at $z = 0$ in the CW run lies either within the WHIM temperature range for $10 \lesssim \delta_b \lesssim 100$ or right outside of the star-forming regions for $10^4 \lesssim \delta_b \lesssim 10^5$, where enriched wind particles lose their kinetic energy due to hydrodynamical interactions. As a consequence, in the CW run the WHIM at these overdensities is more enriched than in other runs.

As for the comparison between NW and BH runs (right-hand panels), we note that BH feedback removes a lot of metal-enriched gas from the surroundings of star-forming regions (see also Fig. 2). This explains the lower metallicity of the densest WHIM in the BH simulation (upper left-hand panel). Furthermore, the suppression of star formation in the BH run also reduces the enrichment level of the shocked gas within collapsed regions with $10^2 \lesssim \delta_b \lesssim 10^3$. At the same time, BH feedback is quite effective in increasing the metallicity of gas lying outside virialized structures, down to rather low densities, $\delta_b \lesssim 10$. The reason for this widespread enrichment is the high efficiency of BH feedback to displace highly enriched gas from the haloes of large galaxies in the redshift range $z \simeq 2$–4, in correspondence with the peak of the BH accretion rate.

As for the dependence of the WHIM metallicity on temperature, the NW and BH runs provide similar trends, with a lower level on enrichment in the BH run.

In general, the results of our simulations confirm that different feedback models leave distinct signatures in the metallicity structure of the WHIM. While these results have in principle interesting implications for the observational characterization of WHIM, it must be emphasized that the large scatter expected in the metallicity distributions requires that metallicity measurements should be carried out for a fairly large number of lines of sight. We defer to a future paper the presentation of an observationally oriented analysis of our simulations, where we discuss the efficiency with which the metallicity structure of the WHIM can be recovered from mock absorption spectra of background sources.

3.5 Evolution of the relative metal abundances

While the above analysis was aimed at describing the overall metallicity of the different gas phases, a much richer amount of information is provided by our chemodynamical simulations. Indeed, the possibility of tracing the enrichment of different elements allows us to study differences in the timing of enrichment of different heavy elements. In this section we explore the redshift evolution of the ratios between the abundances of oxygen with respect to iron and to carbon, with the purpose of quantifying the signatures that IMF and feedback mechanisms leave on the WHIM enrichment history. Atomic transitions associated with these three elements are often used to reveal the presence of the diffuse IGM and to measure its enrichment level at different redshifts. For instance, C v, O vi and O vii lines are considered as the most prominent absorption features in the FUV and soft X-ray spectra of background sources to reveal the presence of the WHIM in the nearby Universe (e.g. Richter et al. 2008, for a review). At the same time, C iii, C iv and O vi absorption lines are commonly used to trace the metal content of the IGM at $z \gtrsim 2$ (e.g. Schaye et al. 2003; Pieri & Haehnelt 2004). Finally, emission features associated with the O viii line and with the Fe–L and Fe–K complexes are used to trace the metal content of the intracluster and intragroup media (e.g. Werner et al. 2008, for a review).

Since different elements are produced in different proportions by different stellar populations, the evolution of their relative abundances is expected to depend, for a fixed mass-dependent lifetime function, on the shape of the stellar IMF (e.g. Tornatore et al. 2007; see Borgani et al. 2008 for a review; Wiersma et al. 2009). In general, we expect that different spatial distributions characterize the enrichment pattern for different elements. As an example, products of SN-II are released over a shorter time-scale than those arising from SN-Ia. Since star particles are expected to move from their original location where they have formed, e.g. due to merging or stripping processes, we expect that SN-II products pollute gas particles lying very close to star-forming regions, while SN-Ia products should have a relatively more diffuse distribution. We expect this effect to be more apparent in the dense environment of galaxy clusters where a population of diffuse intergalactic stars is generated by dynamical processes. Indeed, Tornatore et al. (2007) found from chemodynamical simulations of galaxy clusters that the distribution within the intracluster medium (ICM) of the metals produced by SN-II is more clumpy than that provided by SN-Ia, a prediction that has been also confirmed by observational data (Sivanandam et al. 2009).

In Fig. 10, we plot the [C/O] and [O/Fe] ratios[2] as a function of redshifts for the four models and for both the warm (left-hand panels) and WHIM (right-hand panels) phases. These three elements are produced in different proportions by SN-II and SN-Ia: oxygen is almost entirely produced by SN-II and iron is largely provided by SN-Ia while carbon is produced in comparable proportions by SN-II and SN-Ia; the main contributors to it at a time-scale comparable to that of SN-Ia are AGB stars. The [C/O] ratio has been widely investigated in a variety of environments from dwarf galaxies (Garnett et al. 1995) to low-redshift IGM as probed by quasi-stellar object (QSO) absorption lines (Danforth & Shull 2008), to high-redshift IGM at $z = 2$–4 (Aguirre et al. 2008). As for the [O/Fe] ratio, it is traced in emission with X-ray spectroscopy of relatively poor galaxy clusters and groups (e.g. Rasmussen & Ponman 2007) and is used to study the relative role played by SN-II and SN-Ia in enriching the ICM.

Despite the fact that different feedback prescriptions induce rather different evolutions for the [C/O] ratio, especially for the WHIM phase, the values attained at $z = 0$ are rather similar for all the simulations. We find [C/O] $\simeq -0.2$ and [C/O] $\simeq -0.15$ for the warm and for the WHIM phases, respectively. These values can be compared with a similar analysis of chemodynamical simulations performed by Oppenheimer & Davé (2008). At $z = 0$ they found [C/O] $\simeq -0.09$ and [C/O] $\simeq -0.05$ for the warm and warm-hot phases, respectively, thus about 0.1 dex higher than our results (note that we rescaled their Anders & Grevesse 1989 abundances to our used values). A possible reason for this difference is that Oppenheimer & Davé (2008) used a model for momentum-driven galactic ejecta. However, since they obtain rather stable results for a variety of feedback schemes, it is not clear whether this is a likely explanation for the difference. Another possibility lies in the different sets of yields, mass limit for the SN-II progenitors ($10\,M_\odot$ instead of $8\,M_\odot$ as in our simulations) and the mass-dependent lifetime function adopted by Oppenheimer & Davé (2008). For instance, assuming a larger limiting mass for SN-II turns into a relatively lower amount of oxygen produced, which could explain the larger value of [C/O] found by Oppenheimer & Davé (2008).

As for the evolution of the WHIM phase in the BH run, we note that [C/O] is very close to the NW values at high redshift. This is expected since at early times, BH accretion is quite ineffective.

---

[2] Following a standard notation, we define the relative abundance between the elements X and Y as $[X/Y] = \log(Z_X/Z_Y) - \log(Z_{X,\odot}/Z_{Y,\odot})$.
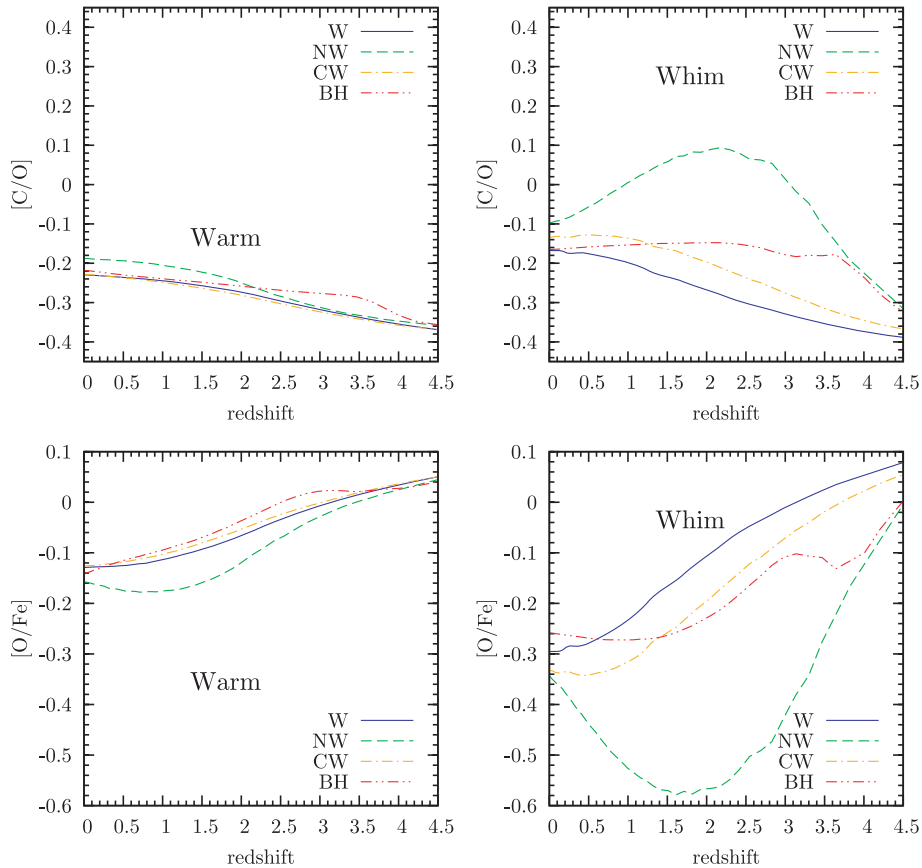
Figure 10. Evolution of the mean value of the [C/O] (upper panels) and [O/Fe] (lower panels) ratios for the warm (left-hand panels) and WHIM (right-hand panels) phases. Each panel shows the results for the $W_{256,37}$, $NW_{256,37}$, $CW_{256,37}$ and $BH_{256,37}$ simulations, represented by the continuous blue, dashed green, dot–dashed orange and double-dot–dashed red lines, respectively.

At these high redshifts, gas at WHIM temperatures starts involving shock-heated gas in filaments. This diffuse gas has been relatively more enriched by long-lived stars that had time to move away from the highest density star-forming regions. This explains why the relative abundance of carbon increases with respect to oxygen, a trend that extends in the NW run down to $z \simeq 2$, when a nearly solar relative abundance is attained. After this redshift, the diffuse gas whose temperature reaches the WHIM values has a progressively lower degree of enrichment. At the same time, the large amount of low-redshift star formation in the absence of feedback causes a prompt release of oxygen from short-lived stars, thus motivating the gentle decline of the [C/O] ratio. As for the run with BH feedback, the WHIM starts receiving at $z \simeq 3.5$ a significant contribution from gas expelled from haloes where gas accretion on to BHs reaches the peak of its efficiency (see also the central panel of Fig. 3). At lower redshift the star formation is strongly quenched in the BH run, thus explaining the substantial flattening of [C/O] for both the warm and the WHIM phases.

The evolution of the [C/O] ratio for the CW and W simulations is similar for the warm and the WHIM phases, for which it rises gently by 0.1 and 0.2 dex, respectively, from $z = 4$ to $z = 0$. Differently from the BH feedback, winds already start affecting the level of star formation at high redshift, $z > 4$. This explains the slower increase of [C/O], which extends down to low redshift, for both the warm and the WHIM phases. While the W and CW runs provide very similar results for the warm phase, the tendency of the decoupled winds to transport more efficiently enriched gas outside haloes justifies the

slightly larger values of [C/O] in the WHIM phase, as found in the CW simulation.

The values obtained at $z = 2$–4 can be compared with those inferred for the IGM by Aguirre et al. (2008) using the pixel-optical depth technique in high-resolution QSO spectra. Their findings of course depend on the strength and shape of the assumed UV background. For a background which is made by galaxies and quasars, they find [C/O] $= -0.7 \pm 0.2$ [this value refers to Anders & Grevesse (1989) abundances and the reported error bar corresponds to systematic uncertainties], which is in reasonable agreement with the results of the warm phase (left-hand panel) that better samples the relatively low-density IGM. From the analysis made by Danforth & Shull (2008), using absorption lines in the low-redshift IGM, values of [C/O] in the range $[-1, 0]$ can be inferred, depending on which ion is used as a tracer of the metallicity. This result is again in broad agreement with the results of our simulations.

Since oxygen is mostly contributed by SN-II, the behaviour of the [O/Fe] ratio has the opposite trend compared to [C/O], with an even more pronounced redshift dependence. The decreasing trend at low redshift is due to the fact that Fe is primarily produced by SN-Ia that has long-lived progenitors. The values of [O/Fe] at $z = 0$ are ~ -0.15 for the warm phase and ~ -0.3 for the WHIM. At $z > 3$, this abundance ratio approaches the solar value. Our findings are in good agreement with the [O/Fe] ratios of gas particles in the ICM of isolated clusters of Tornatore et al. (2007); in particular, values of -0.2 are reached in the outer parts of galaxy clusters and this is close to the value of the WHIM [O/Fe] ratio. As for the
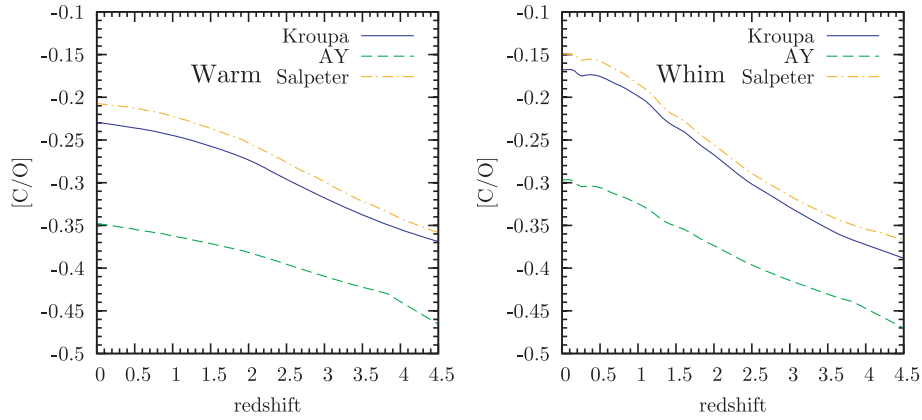
Figure 11. The effect of changing the IMF on the evolution of the [C/O] ratio for the warm (left-hand panel) and WHIM (right-hand panel) phases. The solid blue curves are for the reference run based on the IMF by (Kroupa 2001) ($W_{37,256}$ run), the dashed green curves are for the top-heavy IMF by (Arimoto & Yoshii 1987) ($Way_{37,256}$ run) and the dot–dashed orange curves are for the IMF by (Salpeter 1955) ($Ws_{37,256}$ run).

comparison with the results by Oppenheimer & Davé (2008), we note that our predicted values of [O/Fe] are about 0.4 dex smaller than their WHIM and warm phases once we consider the difference in abundances used. These differences highlight the need to carry out detailed comparison between chemodynamical codes to distinguish the effect of the different implementation of the chemical evolution model from the effect of the different feedback models introduced and of the prescriptions to distribute metals around star-forming regions.

As a final analysis, we verified the effect of changing the IMF on the resulting evolution of [C/O]. Since the slope of the IMF determines the frequency of different SN types, we expect that a top-heavier IMF provides a relatively larger number of SN-II and, therefore, a correspondingly lower value of [C/O]. This is indeed confirmed by the results in Fig. 11, which show a lower value of C/O. A difference of about 0.15 dex is found for the top-heavy IMF by Arimoto & Yoshii (1987), for both the warm and the WHIM phases, while no sizable differences exist between the Kroupa (2001) and Salpeter (1955) IMFs. It is interesting to note that whereas using a top-heavier IMF changes the value of [C/O], its redshift dependence remains essentially unchanged. As such, the effect of changing the IMF is different from the effect of changing the feedback model, which instead does change the evolutionary pattern of the relative abundances.

The main conclusion of this section is that, in spite of the dramatic differences in the feedback schemes and star formation histories, the C/O and O/Fe ratios conspire to reach comparable values at $z = 0$ for all the simulations, with variations of about 20–25 per cent. Larger differences, of up to a factor of $\simeq 2.5$, are instead found at higher redshift, $z = 2.5$. Much smaller differences in the evolution of the relative abundances are instead found by changing the IMF. This implies that an observational determination of the [C/O] evolution would provide information about the nature of the feedback mechanism responsible for regulating star formation and distributing metals.

4 CONCLUSIONS

We have presented results from an extended set of chemodynamical simulations which have been carried out with the GADGET-2 code (Springel 2005), including the implementation of chemical evolution described by Tornatore et al. (2007). The analysis presented here was focused primarily on the low-redshift properties of

the IGM and its evolutionary properties, by considering gas both in a warm phase (gas particles with temperature in the range of 10^4–10^5 K) and in the so-called WHIM phase (gas particles with temperature in the range of 10^5–10^7 K). The main purpose of the analysis was to quantify the effect that different feedback mechanisms leave in the pattern of metal enrichment. Besides a simulation not including any efficient feedback (NW run), we performed simulations including energy feedback resulting from accretion on to SMBHs (BH run; Di Matteo et al. 2005; Springel et al. 2005) and from galactic winds powered by SN explosions. We considered two implementations of the latter, based either on locally decoupling winds from hydrodynamics, so as to allow them to leave star-forming regions (W runs), or on keeping gas in the winds always hydrodynamically coupled with the surrounding medium (CW runs).

The main results of our analysis can be summarized as follows.

(i) The temperature–density and metallicity–density phase diagrams at $z = 0$ are affected by the different feedback prescriptions. Including galactic winds has the effect of enriching with metals the low-density IGM. BH feedback is even more effective than winds in transporting metal-enriched gas from the star-forming regions to the WHIM phase. BH feedback also causes the presence of a non-negligible amount of relatively low-density, metal-enriched hot gas (10^6–10^7 K) which is not present in the simulations with galactic winds.

(ii) The fraction of baryonic mass associated with warm gas, with $T = 10^4$–10^5 K, which should be associated with UV/Lyman α absorption systems, varies from $\gtrsim 90$ per cent at high redshift, $z > 3.5$, to about 30 per cent in the local universe, with a weak dependence on the adopted feedback model. This is in agreement with recent observational estimates from UV spectroscopy (e.g. Danforth & Shull 2008). The hot phase, with $T > 10^7$ K, sums up to 3 per cent at $z = 0$, again almost independent of the feedback model. The fraction of baryons in stars is instead most sensitive to feedback: it ranges from about 10 per cent in the run with no feedback (NW) to about 2 per cent in the run with BH feedback.

(iii) The WHIM phase comprises about 35 per cent of the baryon budget at $z = 0$ for the NW run, a value that increases to about 50 per cent for the run with BH feedback. This confirms that the share of cosmic baryons in the different phases does depend on the assumed feedback model. The redshift evolution of the mass fraction in the

WHIM also differs in the different runs, with a stronger evolution in the run with BH feedback.

(iv) The average age of enrichment of the warm and of the WHIM phases differs in the different runs, by an amount which depends on the gas overdensity δ_b. Diffuse gas ($\delta_b < 50$) in the warm phase at $z = 0$ is typically enriched 0.5–1 Gyr earlier than in the WHIM phase. As for the gas within 'collapsed' regions, with $\delta_b > 50$, the warm phase is enriched 1 Gyr after the WHIM phase in all runs not including BH feedback. In the BH run, enrichment of the densest WHIM as measured at $z = 0$ takes place more than 1.5 Gyr after that of the warm medium. BHs enrich the WHIM more promptly than W in the redshift range $2 \lesssim z \lesssim 4$. On the other hand, winds are more effective at higher redshift, when BH accretion is still inefficient, and below $z \sim 2$, when star formation in the BH run has been quenched. At all epochs, the hydrodynamically coupled winds (CW run) provide a slightly more recent enrichment of both warm and WHIM phases when compared to hydro-decoupled winds (W run). BH feedback provides a faster enrichment at $z > 2$, while below this redshift winds provide a more prompt WHIM enrichment. In particular, the model with hydrodynamically coupled winds (CW) provides at $z < 3$ the most prompt enrichment of both warm and WHIM phases.

(v) In order to address the multiphase nature of the WHIM, we compute the distribution of gas and metals in the WHIM phase as a function of overdensity. As a result of the strong heating provided by BH feedback at $z \simeq 2$–4, the characteristic density of the WHIM in the BH run is a factor of a few lower than in the other simulations and, correspondingly, a smaller amount of gas is present in the dense WHIM. The same trend is also visible for the number of metals present in the WHIM. Typically, most of the metals lie at over-densities between a few and 10 in the run with BH feedback, while the typical density of the metal-enriched gas is about two orders of magnitude higher in the run with galactic winds. The reason for this is that most of the metals are ejected by BH heating from galaxies between $z = 4$ and $z = 2$. The high entropy level reached by enriched gas heated by BH feedback makes hard for it to be reaccreted within collapsed haloes at lower redshift. In turn, the drop of star formation in the BH run causes a comparable suppression of metal production at $z < 2$.

(vi) Underdense WHIM regions (voids) have a very low median metallicity; however, the metallicity of individual gas particles can reach values larger than $0.1 \, Z_\odot$ within the 90 percentile. These enriched particles have been transported to underdense regions both by galactic ejecta and by the action of gas-dynamical processes. Due to the intrinsic lack of diffusion in SPH, such particles spuriously preserve their high-metal content, rather than diffusing metals to surrounding metal-poor particles.

(vii) The values of the [C/O] and [O/Fe] relative abundances at $z = 0$ are similar for both the WHIM and warm phases, also irrespective of the feedback model. Their evolutionary pattern is instead sensitive to the adopted feedback model. Using a top-heavier IMF decreases the value of the [C/O] ratio by about 0.15 dex at all redshifts.

The simulations presented in this paper have been analysed to study separately the effects that SN-triggered winds and BH energy feedback have on the evolution of the IGM. Clearly, in a realistic situation one expects SN and AGN feedback to be both at work and to cooperate in determining the cosmic cycle of baryons. However, we point out that our analysis was not aimed at establishing a best-fitting feedback model, which is able to reproduce a variety of observational results. We instead aimed at determining the imprints that different feedback models leave on the properties of the IGM and their possible observational signatures. Furthermore, it is worth reminding that the parameters that we adopted for winds and BH feedback have been fixed by requiring each of these two feedback sources to reproduce a specific observational constraint: the cosmic SFR for winds (Springel & Hernquist 2003) and the M_{BH}–σ relation for BH feedback (Di Matteo et al. 2005). Once the two mechanisms are allowed to be both present in a simulation, they are expected to have non-trivial interplays, which necessarily require a recalibration of their characteristic parameters.

The results obtained from our analysis have interesting implications for the detectability of the WHIM and for the possibility of characterizing its thermal and chemical properties (e.g. Stocke et al. 2007). Indeed, the possibility of detecting the WHIM through absorption lines in the spectra of background sources does not only depend on the amount of mass in this phase, but also on how this mass is enriched and distributed in density and temperature. With our analysis, we have demonstrated that such distributions are rather sensitive to the adopted scheme of energy feedback. Analyses aimed at discussing the WHIM detectability from simulations, both in emission (e.g. Yoshikawa et al. 2004) and in absorption (e.g. Cen et al. 2001; Viel et al. 2005), have been so far based on approximate descriptions of the pattern of chemical enrichment. We will present in a future paper an observationally oriented analysis of our simulations, aimed at quantifying how the WHIM properties can be recovered under realistic observational conditions in the presence of different feedback schemes. There is no doubt that the possibility of performing high-resolution spectroscopy both in the X-ray (e.g. with micro-calorimeters onboard of large collecting area X-ray telescopes) and in the UV band (i.e. the now operating Cosmic Origin Spectrograph onboard of *Hubble Space Telescope*) will provide a leap forward in the study of the diffuse warm-hot baryons in the local universe. Cosmological hydrodynamical simulations, like those presented in this paper, offer the natural interpretive framework for these future observations, which will not only complete the census of baryons at low redshift but also characterize their physical properties.

REFERENCES

Aguirre A., Dow-Hygelund C., Schaye J., Theuns T., 2008, ApJ, 689, 851
Anders E., Grevesse N., 1989, Geochimica Cosmochimica Acta, 53, 197
Arimoto N., Yoshii Y., 1987, A&A, 173, 23
Asplund M., Grevesse N., Sauval A. J., 2005, in Barnes T. G. III, Bash F. N., eds, ASP Conf. Ser. Vol. 336, Cosmic Abundances as Records of Stellar Evolution and Nucleosynthesis, The Solar Chemical Composition. Astron. Soc. Pac., San Francisco, p. 25
Bertone S., Schaye J., Dolag K., 2008, Space Sci. Rev., 134, 295
Bhattacharya S., di Matteo T., Kosowsky A., 2008, MNRAS, 389, 34

Bolton J. S., Haehnelt M. G., Viel M., Springel V., 2005, MNRAS, 357, 1178

Bondi H., 1952, MNRAS, 112, 195

Borgani S., Fabjan D., Tornatore L., Schindler S., Dolag K., Diaferio A., 2008, Space Sci. Rev., 134, 379

Bouwens R. J., Illingworth G. D., Franx M., Ford H., 2008, ApJ, 686, 230

Branchini E. et al., 2009, ApJ, 697, 328

Buote D. A., Zappacosta L., Fang T., Humphrey P. J., Gastaldello F., Tagliaferri G., 2009, ApJ, 695, 1351

Cen R., Ostriker J. P., 1999, ApJ, 514, 1

Cen R., Ostriker J. P., 2006, ApJ, 650, 560

Cen R., Tripp T. M., Ostriker J. P., Jenkins E. B., 2001, ApJ, 559, L5

Chabrier G., 2003, PASP, 115, 763

Chen X., Weinberg D. H., Katz N., Davé R., 2003, ApJ, 594, 42

Dalla Vecchia C., Schaye J., 2008, MNRAS, 387, 1431

Danforth C. W., Shull J. M., 2008, ApJ, 679, 194

Davé R., Oppenheimer B. D., 2007, MNRAS, 374, 427

Davé R. et al., 2001, ApJ, 552, 473

Di Matteo T., Springel V., Hernquist L., 2005, Nat, 433, 604

Di Matteo T., Colberg J., Springel V., Hernquist L., Sijacki D., 2008, ApJ, 676, 33

Fabjan D., Tornatore L., Borgani S., Saro A., Dolag K., 2008, MNRAS, 386, 1265

Fabjan D., Borgani S., Tornatore L., Saro A., Murante G., Dolag K., 2009, MNRAS, doi:10.1111/j.1365-2966.2009.15794.x

Fiore F. et al., 2000, New Astron., 5, 143

Fukugita M., Peebles P. J. E., 2004, ApJ, 616, 643

Fukugita M., Hogan C. J., Peebles P. J. E., 1998, ApJ, 503, 518

Garnett D. R., Skillman E. D., Dufour R. J., Peimbert M., Torres-Peimbert S., Terlevich R., Terlevich E., Shields G. A., 1995, ApJ, 443, 64

Greif T. H., Glover S. C. O., Bromm V., Klessen R. S., 2009, MNRAS, 392, 1381

Haardt F., Madau P., 1996, ApJ, 461, 20

Hopkins A. M., 2004, ApJ, 615, 209

Kaastra J. S., Werner N., Herder J. W. A. D., Paerels F. B. S., de Plaa J., Rasmussen A. P., de Vries C. P., 2006, ApJ, 652, 189

Katz N., Weinberg D. H., Hernquist L., 1996, ApJS, 105, 19

Kobayashi C., Springel V., White S. D. M., 2007, MNRAS, 376, 1465

Komatsu E. et al., 2009, ApJS, 180, 330

Kravtsov A. V., Klypin A., Hoffman Y., 2002, ApJ, 571, 563

Kroupa P., 2001, MNRAS, 322, 231

Li C., White S. D. M., 2009, MNRAS, 398, 2177

Murray N., Quataert E., Thompson T. A., 2005, ApJ, 618, 569

Nagamine K., Wolfe A. M., Hernquist L., Springel V., 2007, ApJ, 660, 945

Nicastro F. et al., 2005, ApJ, 629, 700

Oppenheimer B. D., Davé R., 2008, MNRAS, 387, 577

Padovani P., Matteucci F., 1993, ApJ, 416, 26

Persic M., Salucci P., 1992, MNRAS, 258, 14P

Pieri M. M., Haehnelt M. G., 2004, MNRAS, 347, 985

Pierleoni M., Branchini E., Viel M., 2008, MNRAS, 388, 282

Puchwein E., Sijacki D., Springel V., 2008, ApJ, 687, L53

Rasmussen J., Ponman T. J., 2007, MNRAS, 380, 1554

Rasmussen A. P., Kahn S. M., Paerels F., Herder J. W. D., Kaastra J., de Vries C., 2007, ApJ, 656, 129

Richter P., Paerels F. B. S., Kaastra J. S., 2008, Space Sci. Rev., 134, 25

Roncarelli M., Moscardini L., Tozzi P., Borgani S., Cheng L. M., Diaferio A., Dolag K., Murante G., 2006, MNRAS, 368, 74

Salpeter E. E., 1955, ApJ, 121, 161

Saro A., Borgani S., Tornatore L., Dolag K., Murante G., Biviano A., Calura F., Charlot S., 2006, MNRAS, 373, 397

Schaye J., Aguirre A., Kim T.-S., Theuns T., Rauch M., Sargent W. L. W., 2003, ApJ, 596, 768

Seljak U., Zaldarriaga M., 1996, ApJ, 469, 437

Shakura N. I., Sunyaev R. A., 1973, A&A, 24, 337

Sijacki D., Springel V., di Matteo T., Hernquist L., 2007, MNRAS, 380, 877

Sijacki D., Pfrommer C., Springel V., Enßlin T. A., 2008, MNRAS, 387, 1403

Sivanandam S., Zabludoff A. I., Zaritsky D., Gonzalez A. H., Kelson D. D., 2009, ApJ, 691, 1787

Springel V., 2005, MNRAS, 364, 1105

Springel V., Hernquist L., 2003, MNRAS, 339, 289

Springel V., Di Matteo T., Hernquist L., 2005, MNRAS, 361, 776

Stocke J. T., Danforth C. W., Shull J. M., Penton S. V., Giroux M. L., 2007, ApJ, 671, 146

Sutherland R. S., Dopita M. A., 1993, ApJS, 88, 253

Tescari E., Viel M., Tornatore L., Borgani S., 2009, MNRAS, 397, 411

Thielemann F.-K. et al., 2003, Nuclear Phys. A, 718, 139

Tornatore L., Borgani S., Dolag K., Matteucci F., 2007, MNRAS, 382, 1050

Tripp T. M., Sembach K. R., Bowen D. V., Savage B. D., Jenkins E. B., Lehner N., Richter P., 2008, ApJS, 177, 39

Ursino E., Galeazzi M., 2006, ApJ, 652, 1085

van den Hoek L. B., Groenewegen M. A. T., 1997, A&AS, 123, 305

Viel M., Branchini E., Cen R., Matarrese S., Mazzotta P., Ostriker J. P., 2003, MNRAS, 341, 792

Viel M., Branchini E., Cen R., Ostriker J. P., Matarrese S., Mazzotta P., Tully B., 2005, MNRAS, 360, 1110

Werner N., Finoguenov A., Kaastra J. S., Simionescu A., Dietrich J. P., Vink J., Böhringer H., 2008, A&A, 482, L29

Wiersma R. P. C., Schaye J., Theuns T., Dalla Vecchia C., Tornatore L., 2009, MNRAS, 399, 574

Woosley S. E., Weaver T. A., 1995, ApJS, 101, 181

Yoshikawa K. et al., 2004, Publ. Astron. Soc. Japan, 56, 939

Zappacosta L., Maiolino R., Mannucci F., Gilli R., Schuecker P., 2005, MNRAS, 357, 929

This paper has been typeset from a TEX/LATEX file prepared by the author.